Optical Properties of Nanohole Arrays in Metal–Dielectric Double Films Prepared by Mask-on-Metal Colloidal Lithography

Juliane Junesch,[†] Takumi Sannomiya,[‡] and Andreas B. Dahlin[§,*]

[†]Laboratory of Biosensors and Bioelectronics, Institute for Biomedical Engineering, Swiss Federal Institute of Technology, Zurich, Switzerland, [‡]Department of Metallurgy and Ceramics Science, Tokyo Institute of Technology, Tokyo, Japan, and [§]Division of Bionanophotonics, Department of Applied Physics, Chalmers University of Technology, Göteborg, Sweden

ABSTRACT We present the fabrication and optical characterization of plasmonic nanostructures consisting of nanohole arrays in two thin films, a metal and a dielectric. A novel method called mask-on-metal colloidal lithography is used to prepare high aspect ratio holes, providing efficient mass fabrication of stable structures with close to vertical walls and without the need for an adhesion layer under the metal. Our approach for understanding the transmission properties is based on solving the dispersions of the guided modes supported by the two films and calculating the influence from interference. The methodology is generic and can be extended to multilayered films. In particular, the influence from coupling to waveguide modes is discussed. We show that by rational design of structural dimensions it is possible to study only bonding surface plasmons and the associated hole transmission maximum. Further, numerical simulations with the multiple multipole program provide good agreement with experimental data and enable visualization of the asymmetric near-field distribution in the nanohole arrays, which is focused to the interior of the "nanowells". The refractometric sensitivity is evaluated experimentally both by liquid bulk changes and surface adsorption. We demonstrate how the localized mode provides reasonably good sensitivity in terms of resonance shift to molecular binding inside the voids. Importantly, high resolution sensing can be accomplished also for the surface plasmon mode, despite its extremely low figure of merit. This is accomplished by monitoring the coupling efficiency of light to plasmons instead of conventional sensing which is based on changes in plasmon energy. We suggest that these nanohole structures can be used for studying molecular transport through nanopores and the behavior of molecules confined in volumes of approximately one attoliter.

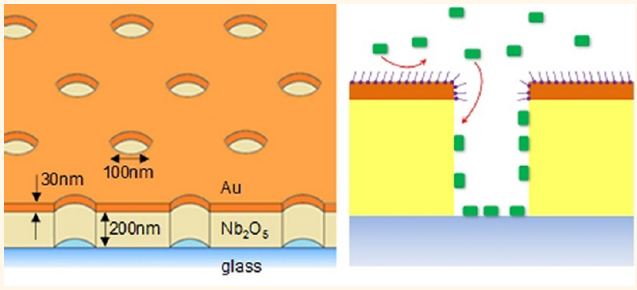

KEYWORDS: plasmon · nanohole array · thin film · metal · dielectric · waveguide

The broad and interdisciplinary research field of plasmonics was established with the new millennium and has emerged in strong synergy with advances in nanofabrication technology. The possibility to focus and control electromagnetic fields on the nanoscale has led to the development of several new types of devices.[1−3] One of the most popular areas of application for plasmonics is molecular sensing by local changes in refractive index (RI), that is, refractometric detection.[4] In comparison with conventional surface plasmon resonance (SPR) in planar metal films,[5] plasmonic nanostructures are expected to offer simpler and cheaper detection platforms that are also compatible with extreme miniaturization and single molecule resolution.[6] Much of the research on fabrication and characterization of plasmonic nanostructures for sensing applications has focused on nanoparticles. Since the first work on refractometric sensing with colloidal gold,[7] many new shapes of nanoparticles have been synthesized and investigated.[8] In attempts to enhance the sensitivity further and become competitive with SPR, more complex nanoparticle assemblies that support Fano resonances[9] have been fabricated[10] and nanoparticle-based metamaterials have been used in SPR-like reflection configuration.[11] Also, spectroscopic readout based on phase changes has recently

* Address correspondence to adahlin@chalmers.se.

Received for review October 8, 2012 and accepted October 25, 2012.

Published online October 25, 2012
10.1021/nn304662e

been introduced for nanoparticles, again in order to improve sensitivity.[12] Yet, in most real sensing applications SPR remains the golden standard,[13] arguably because it does not require any nanofabrication and provides excellent resolution in terms of surface coverage (commercial instrument specifications $\approx$ 10 pg/cm^2). Miniaturization of plasmonic sensors through measurements on single nanoparticles does not improve this value.[14]

In contrast to nanoparticles, nanoholes in metal films offer several unique possibilities as refractometric sensors.[15−17] Holes can be used for entrapment of nanoscale objects such as lipid vesicles[18,19] or even plasmonic nanoparticles.[20] The fact that the sensitivity is strongly localized to the interior of the holes[21−24] makes it simple to work with alternate surface chemistry, for instance solid supported lipid membranes.[21] Certain types of nanohole arrays also open up for formation of pore-spanning lipid membranes,[25] which offer compatibility with studies of membrane proteins and transport processes. Further, the continuous metal film enables simple implementation of additional sensing techniques such as piezoelectric excitation[26] or electrochemical control.[27,28] Last but not least, nanoholes can be used as nanochannels in a flow-through configuration,[29−31] which provides efficient delivery of molecules. Although nanohole arrays provide a sensing performance similar to nanoplasmonic sensors utilizing nanoparticles,[16] all these unique advantages motivate further research. Since the discovery of extraordinary transmission,[32] much effort has been spent on understanding the optical properties of nanohole structures in a single metal film.[33] However, there is little work addressing optical properties of nanohole arrays in *multilayers*, that is, the influence of additional thin films. Yet, in many devices, an additional dielectric film is indeed part of the structure, such as the silicon nitride support in flow-through configuration[25,29−31] and additional hard[18,24,34,35] or soft[36] coatings on the metal. Concerning fabrication of more advanced nanohole arrays, attempts have also been made to "elevate" the metal film,[37−39] usually by etching into the underlying support. The motivation is normally that a volume can be liberated for use in refractometric sensing, thereby enhancing the sensitivity by utilizing more of the probing volume. However, no such fabrication technique provides structures with cylindrically shaped voids and planar interfaces. Indeed, vertical walls and precise control of smaller diameters (100 nm) cannot be achieved by isotropic wet etching,[38,39] and even dry etching[30] or focused ion beam[25] tends to produce conical holes. In addition, many fabrication approaches are limited by serial processing and high costs.

Here we take an important step toward understanding nanohole arrays in multilayered films by a coherent study of the case of *two* thin films, one metal and one dielectric. We introduce a new fabrication process that can provide cylindrical holes through both films, without the need of an adhesion layer and with high throughput. To understand the optical properties, we first use Fresnel calculations to determine the influence from Fabry-Pérot interference on the transmission. Next, the dispersion relations for all types of surface waves in the system, including waveguide modes in the dielectric, are solved analytically. We[23] and others[40,41] have shown that short-range ordered (characteristic spacing) hole arrays[42] provide essentially identical optical properties as long-range ordered (fully periodic) arrays, an analogy which is further investigated here. We also perform numerical simulations using the multiple multipole program[23] (MMP) in order to visualize the near field of the structure. The refractometric sensing capabilities of the structure are investigated both in terms of liquid bulk changes and surface binding. Finally, we discuss how to perform spectral analysis for high resolution sensing with this structure.

RESULTS AND DISCUSSION

Nanofabrication. The fabrication process for nanohole arrays in metal−dielectric double films, which we refer to as mask-on-metal colloidal lithography (MoM-CL) is described in Figure 1. The dielectric is first deposited on the support, followed by colloidal self-assembly as described previously.[27,28] Next, the metal film is deposited by physical vapor deposition (PVD), but in addition a mask for dry etching is deposited on the metal (preferably in the same evaporator run). The colloids are then removed by a new lift-off process which is based on rubbing the wetted surface with the edge of a soft material, similar to squeegee polishing. This type of "nanoshaving" has previously been used to remove lipid vesicles from a planar surface.[18] The squeegee was critical for successful fabrication since it was milder and more efficient than the conventional tape lift-off.[42] Next, reactive ion etching (RIE) is used to etch holes that continue into the underlying dielectric. It should be noted that with MoM-CL, etching of the metal is not necessary because the holes are already present in the metal after PVD. Finally, the RIE mask is removed and the samples are thermally annealed to improve stability. The only limitation of MoM-CL is that it cannot be used to prepare thick metal films if the hole diameter should also be small (metal thickness must be below the colloid radius). These process steps were further verified by measuring extinction spectra after each step (Supporting Information).

The MoM-CL is compatible with several materials for the metal and the dielectric films. For the metal, we chose gold (Au) because of its well-known optical properties and high chemical stability. Several dielectrics materials were evaluated, but below we only present results for niobium pentoxide (Nb_2O_5) films prepared by reactive sputtering. This material is known to provide mechanically stable films with low stress

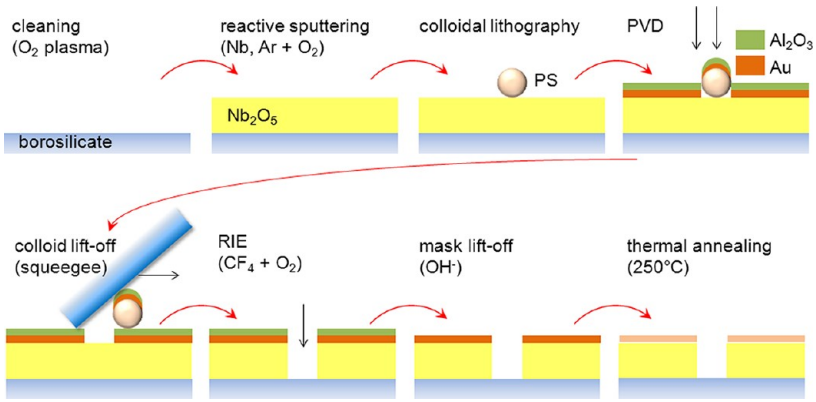

Figure 1. Fabrication of nanohole arrays in metal−dielectric double films by mask-on-metal colloidal lithography. The method is based on colloidal self-assembly and parallel processing of areas of several cm^2. By depositing an additional protective film on top of the metal, the underlying dielectric can be etched anisotropically.

and is also biocompatible. In addition, Nb_2O_5 provides good adhesion to Au, thereby removing the need for an optically lossy adhesion layer (Ti or Cr). Another alternative which does not require an adhesion layer is TiO_2, but for this material we could not achieve an anisotropic etch; that is, the walls were far from vertical. The MoM-CL was also tested with silicon nitride or silicon oxide as dielectrics, but as expected this required an adhesion layer for stability of the Au film. In principle, one can also think of several materials for the mask deposited on the metal (*e.g.*, Al, Ni, Cr, or Ti) which should provide good selectivity toward Nb_2O_5. However, we noted that when using metals as RIE masks, the fabrication fails because of alloy formation with Au during the etch. Instead, we used a thin (20 nm) alumina (Al_2O_3) mask. The thermal annealing step was used to lower the absorption of Au.[27] The relatively low temperature of 250 °C preserved the shape of the holes and is not expected to alter the Nb_2O_5 film significantly.[43,44]

Figure 2 shows scanning electron microscopy (SEM) images of nanohole arrays prepared by MoM-CL. For all samples described in this paper, the Au film was 30 nm thick. Figure 2A shows a large area sample with 100 nm holes (colloids), illustrating that the lithography provides defect-free patterns also when performed on Nb_2O_5. Figure 2B shows the cross section (~90° tilt) of an incompletely etched hole (100 nm diameter and 300 nm Nb_2O_5), indicating the mechanism by which the RIE digs out the dielectric. Figure 2C shows 150 nm holes and 300 nm Nb_2O_5 with the Al_2O_3 mask remaining, after the RIE. Figure 2D shows a scratched and tilted sample surface (also 150 nm holes and 300 nm Nb_2O_5). The SEM images show several results related to the RIE process. First, the Al_2O_3 mask was extremely resistant toward the RIE and protected Au well from above (Figure 2C). Second, the borosilicate glass acts as an efficient etch stop, as verified by the smooth surface appearing under the Nb_2O_5 in Figure 2D. To a small extent, Au is also etched as can be deduced from the top aperture in Figure 2B which is a bit larger than the colloid diameter. Upon reaching the glass, the reactive ions can only etch the walls of the holes. Results from prolonged etching indicated that the holes then grow in diameter and eventually all Nb_2O_5 is removed by etching under Au, resulting in "ordinary" Au hole arrays on glass. Since the RIE is directional but also material selective, the shape of the holes when using MoM-CL is very sensitive to the etch rate/time. An example of holes that are very close to cylindrical is shown in Figure 2D (~5° deviation from 90°). In Figure 2C, the holes are slightly more conical (~10° deviation) as can be seen from the contrast of the exposed glass. We acknowledge that it was difficult to prepare *perfectly* vertical walls in a reliable manner since the etch rate in the RIE was not fully reproducible. Still, we believe these nanoscale voids are much closer to a cylindrical shape than what has been previously presented in the literature.

Optical Characterization. We first emphasize that these samples do not contain "random holes", but display a well-known short-range ordered pattern,[23,27,28,42] which is expected to be equivalent to long-range order in terms of optical properties.[23] The effective periodicity (Λ) of the short-range ordered arrays is simply the characteristic spacing to the nearest neighbors, as determined from the radial distribution function.[23,27,28] We present results from colloids with diameters of 100 and 150 nm that have characteristic spacing values of Λ = 290 nm and Λ = 230 nm, respectively, as shown in the Supporting Information. Extinction spectra (inverse of transmission) of four different Au−Nb_2O_5 nanohole arrays in air are shown in Figure 3. The hole diameter (and thus Λ) is varied together with the thickness of Nb_2O_5 (h_2) which is either 200 or 300 nm. As expected, all samples show the characteristic asymmetric resonance feature in extinction, that is, a maximum accompanied by a minimum at a nearby longer wavelength.[23] However, as we will show in this section, there are additional effects contributing to the spectrum.

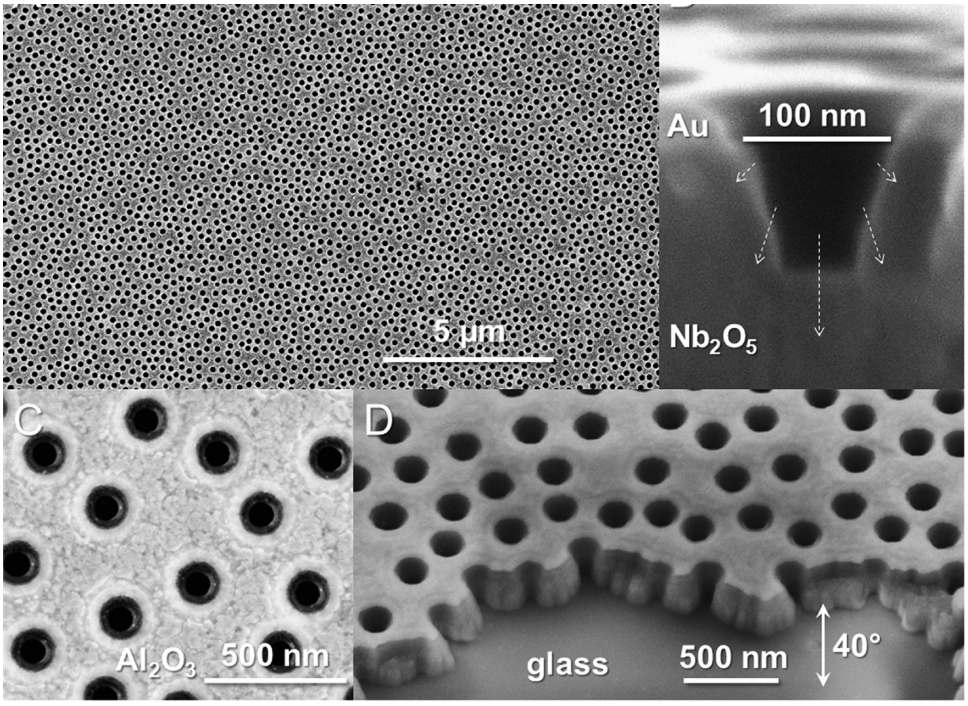

Figure 2. Electron microscopy investigation of fabricated structures: (A) short-range ordered pattern on a large area; (B) cross section of an incompletely etched hole; (C) a sample with the Al_2O_3 mask remaining, after the dry etch; (D) scratched and tilted sample surface.

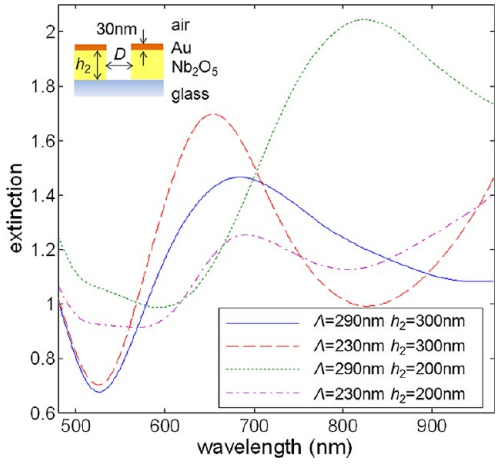

Figure 3. Experimental extinction spectra of four different types of Au−Nb_2O_5 double film nanohole arrays with dimensions described by the inset. For D = 100 nm colloids, the periodicity of the arrays is Λ = 230 nm and for D = 150 nm we have Λ = 290 nm. Spectra were recorded with samples exposed to air.

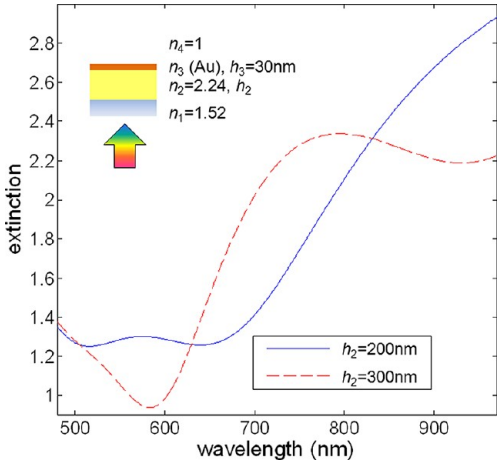

Figure 4. Transfer matrix calculations of the extinction of a two planar film system without holes, for the two different thickness values of Nb_2O_5 investigated. Refractive index values are shown in the inset. Note that the wavelength interval is the same as in Figure 3.

Since we focus on thin Au films (h_3 = 30 nm), these nanohole arrays exhibit high "ordinary transmission" through the metal.[42] The presence of a sufficiently thick and high RI (n_2 = 2.24 for Nb_2O_5) dielectric film in contact with the metal is expected to introduce Fabry−Pérot type interference effects in the transmitted light. Figure 4 shows transfer matrix calculations of the extinction of the corresponding planar film system *without* holes. These calculations agreed very well with experimental spectra of samples that did not contain holes (not shown) and can be used to estimate the influence from interference. It can be seen that the spectral features in the 500−600 nm region (Figure 3), which are in part due to Au absorption, can be reproduced by the calculations (Figure 4) for the different values of h_2. More importantly, for h_2 = 300 nm, interference causes a peak feature in the spectrum very similar to that of plasmon excitation in nanohole arrays.[42] Thus, for the samples with h_2 = 300 nm, the contribution from the nanoholes to the spectrum is hard to distinguish because interference at normal

incidence can generate "false resonances". On the contrary, for $h_2 = 200$ nm, there are no clear peaks resulting from interference since such effects are pushed into the UV region. Although some spectral features remain, this suggests that 200 nm of Nb_2O_5 is preferable if one wants to focus on the optical properties in terms of surface waves that propagate along the thin films (at least for the vis–NIR).

In addition to interference, one must also consider the influence from all different surface waves to which the presence of holes enables coupling. Metal–dielectric double films do not only support surface plasmons, but also planar film waveguide modes.[45] The arbitrary equation for the dispersion relation of surface waves in a four-material, three-interface, and two-film system is given by[28,46]

$$\begin{aligned} 0 = & \left[\frac{\varepsilon_1}{ik_{z1}} - \frac{\varepsilon_2}{ik_{z2}}\right]\left[\frac{\varepsilon_2}{ik_{z2}} - \frac{\varepsilon_3}{ik_{z3}}\right]\left[\frac{\varepsilon_3}{ik_{z3}} - \frac{\varepsilon_4}{ik_{z4}}\right] \\ & + \left[\frac{\varepsilon_1}{ik_{z1}} - \frac{\varepsilon_2}{ik_{z2}}\right]\left[\frac{\varepsilon_2}{ik_{z2}} - \frac{\varepsilon_3}{ik_{z3}}\right]\left[\frac{\varepsilon_3}{ik_{z3}} - \frac{\varepsilon_4}{ik_{z4}}\right] e^{-2ik_{z2}h_2} \\ & + \left[\frac{\varepsilon_1}{ik_{z1}} - \frac{\varepsilon_2}{ik_{z2}}\right]\left[\frac{\varepsilon_2}{ik_{z2}} - \frac{\varepsilon_3}{ik_{z3}}\right]\left[\frac{\varepsilon_3}{ik_{z3}} - \frac{\varepsilon_4}{ik_{z4}}\right] e^{-2ik_{z3}h_3} \\ & + \left[\frac{\varepsilon_1}{ik_{z1}} - \frac{\varepsilon_2}{ik_{z2}}\right]\left[\frac{\varepsilon_2}{ik_{z2}} - \frac{\varepsilon_3}{ik_{z3}}\right]\left[\frac{\varepsilon_3}{ik_{z3}} - \frac{\varepsilon_4}{ik_{z4}}\right] e^{-2i[k_{z2}h_2 + k_{z3}h_3]} \end{aligned} \quad (1)$$

Here 1 and 4 represent the semi-infinite materials, ε is the permittivity of each material (complex for Au), and k_z is the vertical component of the wavevector in each material. We can assume transverse magnetic (TM) polarization so that the magnetic field H obeys

$$\vec{H}(x, z, t) = H_0 e^{i[k_x x + k_z z - \omega t]}\vec{y} \quad (2)$$

For any surface wave, k_x has the same value in each material.[46] Momentum conservation implies that $k_x = [k_0^2 - k_{zj}^2]^{1/2}$ in material j. For the case of waveguide modes, transverse electric (TE) polarization is also possible,[45] in contrast to surface plasmons which are TM.[5] It is straightforward to solve for TE modes instead by modifying the boundary conditions for the field.

The presence of a periodic structure introduces diffractive grating coupling to the surface waves, whether it is a dielectric waveguide mode[36,45] or a surface plasmon.[32] The plasmon resonance/waveguiding excitation condition is that both energy and in-plane wavevector match for photon and surface wave. For normal incidence, all momentum is provided by the periodic structure on the surface. Further, for first order coupling the surface wave should have a wavelength equal to the periodicity of the nanohole array. Thus, the resonance condition is simply

$$\frac{2\pi}{\mathrm{Re}(k_x)} = \wedge \quad (3)$$

Note that none of the equations contain the diameter D of the holes. Since we have the values for Λ (the characteristic spacing) for our MoM-CL nanohole arrays from SEM image analysis, only the dispersion relations are needed to predict the resonant wavelength at which coupling to a surface wave occurs by eq 3.[27,28] We solved eq 1 numerically by using an analytical fit[47] to literature data[48] for the optical properties of Au (ε_3), thereby taking absorption into account. The major challenge is to find *all* the solutions to eq 1 and to *identify* which type of mode that corresponds to which dispersion. For the case of surface plasmons in a finite metal film there are two modes[5,49] which can be referred to as bonding and antibonding surface plasmons.[4,50] These can be identified by utilizing the fact that the antibonding mode has low dissipation, that is, $\mathrm{Im}(k_x)$ is low, and longer field extension into the environment, that is, $\mathrm{Im}(k_{z4})$ is low. Further, in order to simplify interpretation of the results, we also solved the waveguide modes separately using another formalism as described in the Supporting Information.

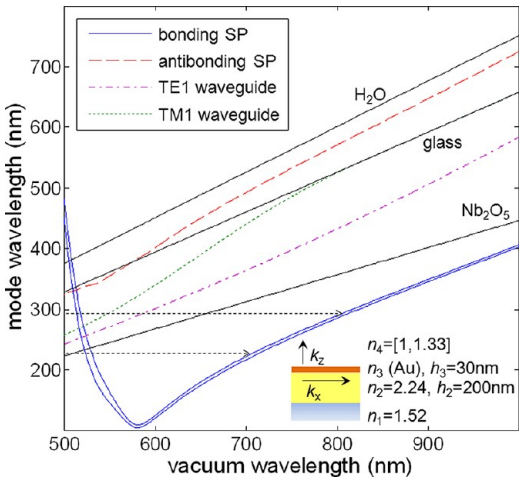

Figure 5. Calculated dispersion relations for the surface waves in a system with four materials, three interfaces, and two thin films as defined by the inset. The dispersions are presented as mode wavelength plotted against vacuum wavelength. For this system, there are two surface plasmon modes and two waveguide modes. All dispersion are calculated in an air environment, but for the bonding surface plasmon the curve for water is also included (solid line shifted slightly down). The photon lines for the dielectrics are also shown. The dashed arrows show the periodicities of the nanohole arrays.

Figure 5 shows the calculated dispersion relations for surface plasmons and waveguide modes in a system with $h_2 = 200$ nm Nb_2O_5 ($n_2 = 2.24$) and $h_3 = 30$ nm Au. The supporting material is glass ($n_1 = 1.52$) and the Au is exposed to air ($n_4 = 1$). We plot the dispersions as wavelength ($2\pi/\mathrm{Re}(k_x)$) *versus* vacuum wavelength ($2\pi/k_0$) for the different modes and include the photon lines for water, glass, and Nb_2O_5. The Nb_2O_5 film only supports first order waveguide modes for this thickness and they appear above the photon line for Nb_2O_5, illustrating total internal reflection inside the dielectric film. The dispersion above the glass line is the antibonding surface plasmon, which is leaky into the higher RI material in contact with Au.[4] Finally, at low

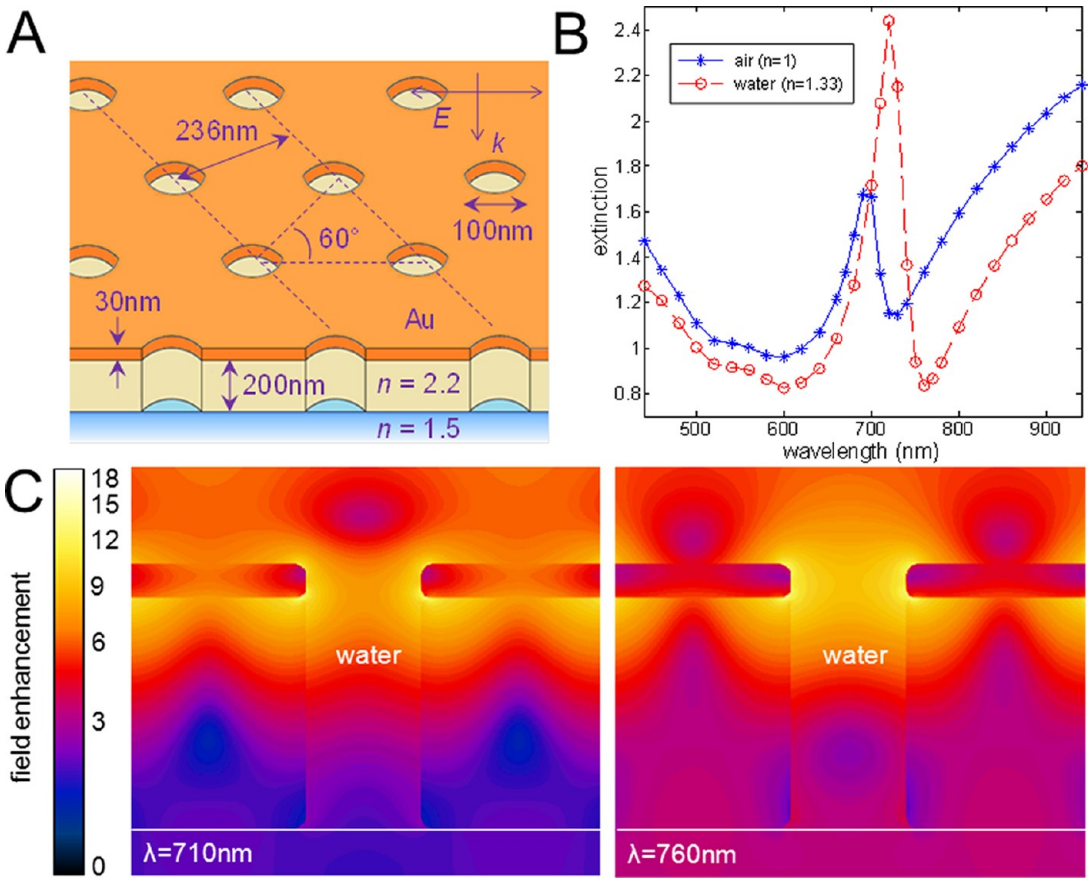

Figure 6. (A) Schematic of simulated near-field and far-field optical properties of a Au−Nb_2O_5 nanohole array; (B) extinction spectra for the surface in contact with air or water; (C) time-averaged field enhancement plots for the case of water at the wavelengths corresponding to the extinction maximum and minimum. The cross section is along the direction of the polarization of the incident wave.

energies the bonding surface plasmon appears (solid lines), for which we also calculate the dispersion in water (n_4 = 1.33), resulting in a curve slightly shifted downward in Figure 5. Next, the resonance condition eq 3 can be utilized by inserting the periodicity values of the arrays on the *y*-axis in Figure 5 (dashed arrows). For Λ = 290 nm (150 nm colloids) Figure 5 predicts coupling to waveguide modes in the 500−600 nm region and coupling to the bonding surface plasmon around 800 nm, which is in good agreement with the extinction peak at ~820 nm in Figure 3. For Λ = 230 nm (100 nm colloids), that is, below the Nb_2O_5 photon line in Figure 5, the dispersions predict coupling only to the bonding surface plasmon around 700 nm, in excellent agreement with the observed extinction peak in Figure 3.

In summary, we have now shown that the vis-NIR spectral features in the transmission through these nanohole arrays have contributions from interference in the thin films, especially for thicker Nb_2O_5, and that there is also a possible influence from coupling to waveguide modes, at least for the higher value of Λ. For thicker dielectric films like h_2 = 300 nm, second order waveguide modes are also supported and the first order modes are further shifted to the red. Thus, it seems likely that for the 150 nm holes, the extinction spectra in Figure 3 should have a significant contribution from waveguides approximately in the 500−700 nm region. This is supported by the extinction increase already below 600 nm because interference should not contribute until above 600 nm (Figure 4). However, all waveguide modes must lie above the Nb_2O_5 photon line in Figure 5. Therefore, for the 100 nm holes (Λ = 230 nm), it is clear that waveguide modes cannot be excited because the periodicity of the hole array generates a k_x vector which is too high in magnitude. Although it is intriguing to further investigate waveguide excitation in these structures, we have chosen to focus on the plasmonic properties in this work. (Coupling to waveguide modes by short-range ordered nanoholes is currently being thoroughly investigated by us in a parallel study.) Thus, for the rest of this paper, the "purely plasmonic" structure with 100 nm holes and 200 nm Nb_2O_5 is investigated.

To visualize the near field in the nanostructure, we performed simulations using MMP (Figure 6). Because of the requirement of periodic boundary conditions in the simulations, a hexagonal hole array was used to represent the short-range ordered samples. As shown here and in previous work,[23] the analogy between

short-range and long-range order validates the use of this approach. Therefore, the structure was modeled as shown in Figure 6A, using an interference length for the plasmon in the hexagonal lattice of 234 nm, that is, essentially the same as the periodicity of Λ = 230 nm. The permittivity of Au was estimated from linear interpolation of literature data points.[48] The full extinction spectrum was calculated in air and water environments (note that here the RI is changed also inside the holes) as shown in Figure 6B. Sharper resonance features are predicted by these calculations mainly because of the idealized conditions in the MMP simulations (infinite periodicity and identical holes), that is, *not* because the simulated arrays exhibit long-range order.[23] In terms of far field properties, the extinction peak position in air is in perfect agreement with the experimental results (Figure 3) and the small shift upon changing to water is comparable to that predicted by the dispersion of the bonding surface plasmon (Figure 5). The nearby extinction minimum appears at a shorter wavelength (~730 nm) in the MMP simulations compared to the experiments (~800 nm). This is expected because the extinction minimum corresponds to a localized void resonance which is very sensitive to the shape and ordering of the holes.[23] The error is thus explained by the fact that the real structure (Figure 2) differs from the idealized shape and periodicity in the MMP (Figure 6A). In contrast, the surface plasmon peak position is sensitive only to the periodicity of the holes,[23] eq 3, whether it is short-range or long-range order.

Figure 6C shows the near field at the extinction maximum and minimum for the case of a water environment. The spatial distribution of the field enhancement is quite similar in both cases but for the extinction peak there is a local minimum in the field just above the Au aperture, while the extinction dip shows a strong field enhancement in general in the upper part of the cylindrical voids. This confirms the surface wave character of the bonding surface plasmon and the localized nature of the transmission maximum. Also, the extension of the field is on average similar for the minimum and maximum. This is explained by the quick field decay of the bonding surface plasmon, which is expected to be comparable to localized plasmons.[26] Further, the near field distribution is highly asymmetric and shifted toward the Nb_2O_5 side of the Au film, as expected due to the high RI contrast between water and Nb_2O_5.[49] Overall, these results suggest that the double film nanohole array structure should provide interesting refractometric sensing properties. It should be especially well suited for detecting molecules inside the nanoscale voids where the asymmetric field is strongly enhanced.

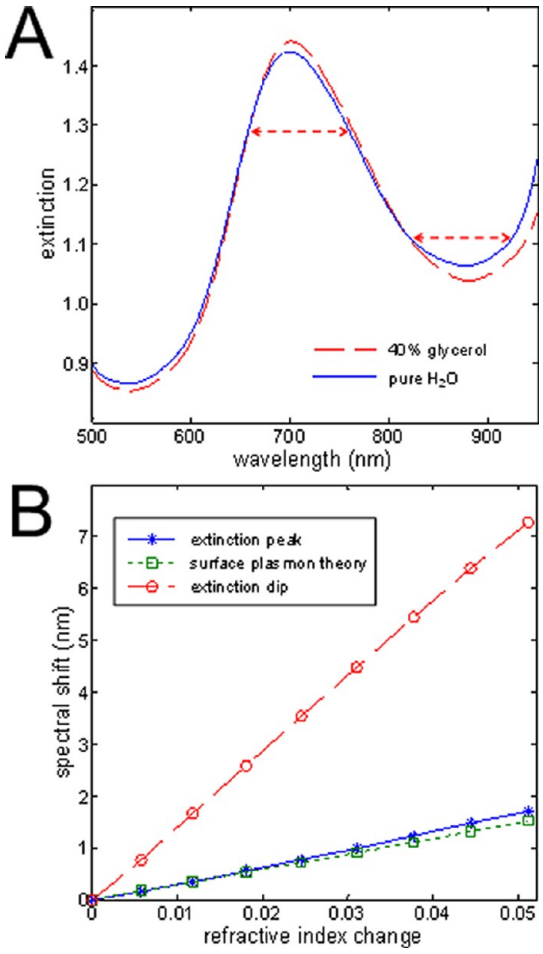

Figure 7. Refractive index sensing with glycerol in water using a 30 nm Au and 200 nm Nb_2O_5 nanohole array with 100 nm holes. (A) Full spectra. The dashed arrows indicate the width of the spans used to estimate the resonance wavelengths. Spectra were measured at 5, 10, 15, 20, 25, 30, 35 and 40% glycerol by mass. (B) Sensitivities in terms of wavelength shifts for the extinction peak (asterisks) and dip (circles). The theoretical shifts for the bonding surface plasmon predicted from the dispersion relation are also shown (squares).

Refractometric Sensing. We focus again on the plasmon resonances in the structure with h_2 = 200 nm Nb_2O_5, h_3 = 30 nm Au, and D = 100 nm holes. For the peak, the changes when going from air to water have already been predicted to be low by the dispersion relation (~7 nm peak shift) and the MMP simulations (Figure 6B). Indeed, as expected by the asymmetric field distribution around the Au film, the sensitivity in terms of extinction peak shift per RI increase is low. As shown in Figure 7A, the peak appears at essentially the same wavelength in water. Figure 7 also shows a more precise calibration of the spectral changes upon increasing the RI of the environment with glycerol in water.[28,51] The extinction maximum and minimum were both monitored and their positions were defined using a 100 nm wavelength span (dashed arrows) for calculating the centroid.[51] The resonance shifts are plotted in Figure 7B, together with the predicted shifts

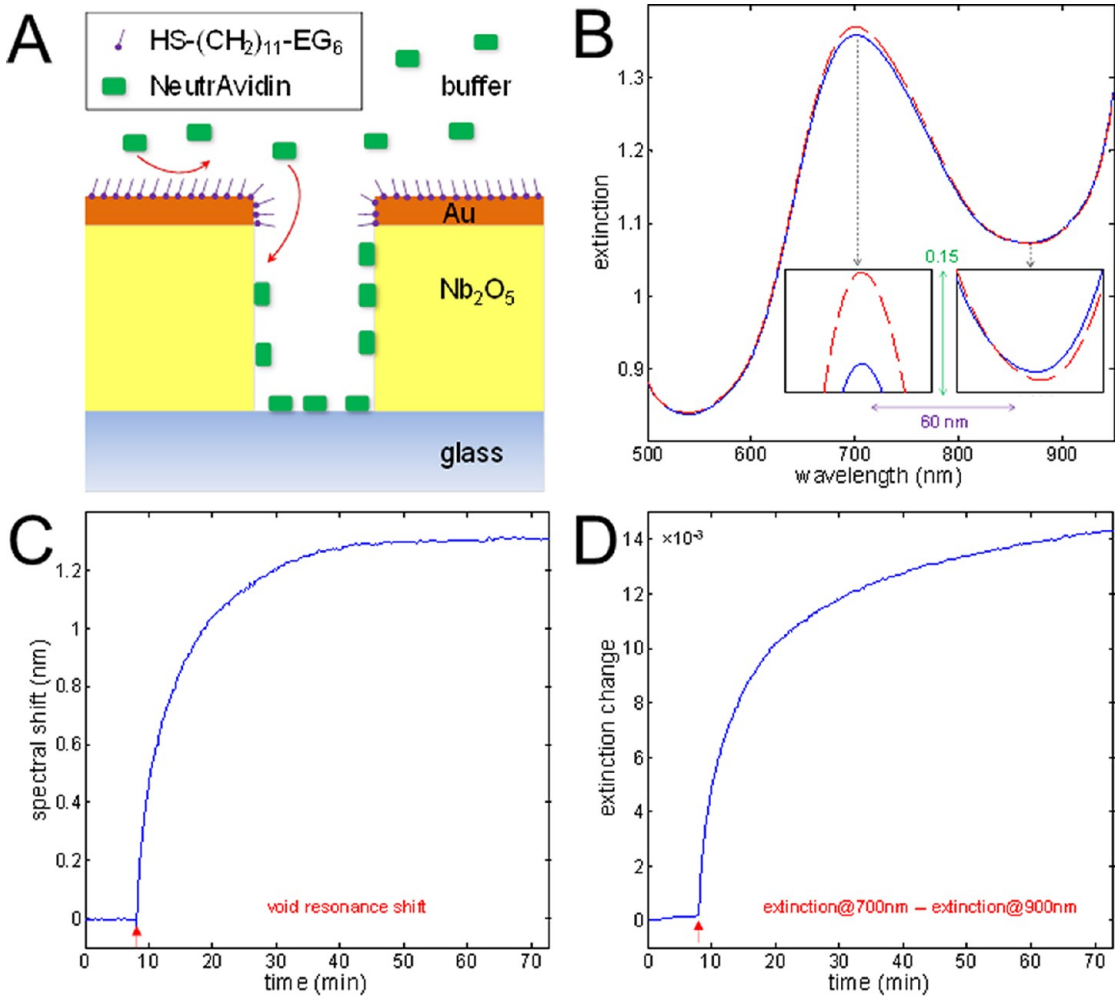

Figure 8. (A) Sensing of protein adsorption inside the nanoholes with the surface functionalized as described in the schematic. Thiol chemistry is used to selectively block Au so that NeutrAvidin adsorbs only inside the holes on the Nb_2O_5 or glass regions. (B) Changes in the full spectrum after saturated adsorption. The insets highlight the changes in the peak and the dip. (C) Redshift of the extinction minimum in real-time (protein added after 8 min); (D) the same adsorption event but in terms of extinction changes. The monitored parameter is the extinction at 700 nm minus the extinction at 900 nm.

from dispersion relation calculations for the bonding surface plasmon. Again, the extinction peak is excellently described by surface plasmon theory, and the low signal in terms of peak shift (34 nm per RI unit) is confirmed. In constrast, the extinction dip shows a higher peak shift of 144 nm per RI unit, which is a typical value for localized resonances, for example, in individual nanoparticles.[28,52] The shift of the extinction minimum also agreed well with the values predicted by MMP (~40 nm air to water).

Next, we evaluate the structure for sensing surface binding events, as summarized in Figure 8. Motivated by the high field enhancement inside the nanoholes (Figure 6C), we used selective chemistry to direct molecules to the Nb_2O_5 walls (and the glass bottom if the holes are deep enough). A short thiolated oligo(ethyleneglycol) (OEG) was specifically bound to Au using established chemistry, making it inert toward biomolecular adsorption.[22] As expected, the OEG binding in ethanol to Au resulted in only a small peak shift of ~0.4 nm. Then, we let a protein (NeutrAvidin, 60 kD) adsorb inside the nanoscale voids (Figure 8A). The surface functionalization with OEG and the material-specific protein adsorption were verified independently by quartz crystal microbalance measurements (data not shown). The spectral changes upon protein adsorption are shown in Figure 8B. Again, only the extinction dip shows a strong shift, which is tracked in real-time in Figure 8C. Thus, the low sensitivity in terms of redshifting for the bonding surface plasmons (extinction peak) in these structures is well compensated for by the fact that the localized mode (extinction dip) maintains good sensitivity. However, the extinction peak can still be utilized for sensing by ignoring redshifts altogether and instead measure the difference between the extinction values at two fixed wavelengths,[51,53] as shown in Figure 8D (700 and 900 nm). We emphasize that here the major cause for the signal, that is, the extinction change, is the peak because it increases so

strongly in magnitude, while the extinction changes associated with the dip are lower (insets in Figure 8B). Notably, this type of spectral analysis is quite different from the conventional approach that aims to measure only the resonance redshift in response to a RI increase.

Next, we wish to discuss the binding curve in Figure 8D in relation to the well-established figure of merit (FoM) parameter, which is currently the benchmark for evaluating the performance of novel nanoplasmonic sensors.[10,12,54] The FoM is calculated as redshift per RI unit divided by peak width, which for the surface plasmon in our structure translates to approximately 0.2. This likely represents the world record in *low* FoM. Yet, utilizing this spectral resonance clearly provides excellent resolution in protein surface coverage (with the appropriate spectral analysis), comparable to the best nanoplasmonic sensors (~0.1 ng/cm^2) even in this unoptimized system. Thus, we suggest that the FoM concept must be used with care since it does not provide the full picture. Indeed, as we have discussed in detail,[4,28,55] changes in relative intensity (*e.g.*, extinction) is what matters in the end for the refractometric sensing performance.

Following this formalism, if one considers the sensitivity in terms of relative intensity changes (instead of redshifts), the new structure has a sensitivity of ~0.41 extinction units per RI unit at the peak (~710 nm). When comparing this value to nanohole arrays of similar dimensions in a single Au film, one sees that the intensity-based sensitivity is actually ~50% higher,[28] even though the FoM is lower than for the "ordinary" structures (typical FoM $\approx$ 1). The higher intensity-based sensitivity is not surprising since a solid volume is liberated under the metal aperture. When changing the liquid RI one can thus expect stronger spectral changes because more of the plasmonic probing volume is available. Also in terms of surface binding, the performance is slightly increased upon etching out the dielectric bottom of the holes. This is because the signal from molecular binding is higher at the Au walls compared to the middle of the apertures, as we have previously shown by experiment[22] and theory.[23] Since the field enhancement continues from the Au quite far down along the Nb_2O_5 walls (Figure 6C) inside these new holes, one can expect a similar signal per molecule as for conventional holes and a higher signal for a saturated monolayer due to the increased surface area.

As a final point, it is interesting to consider the underlying physical mechanism for the high sensitivity in terms of peak magnitude. Apparently, a RI increase inside or just below the metal aperture enhances the *coupling efficiency* to the bonding surface plasmons. This concept differs from the established "plasmonic sensing dogma" which states that the energy of any resonance is lowered in a more optically dense dielectric environment. In principle, any physical mechanism that provides a change in measured intensity as a result of increased RI can be utilized for refractometric sensing and the performance of the sensor depends on the magnitude of those intensity changes.

CONCLUSIONS

We have shown the fabrication and optical characterization of nanohole arrays in metal–dielectric double films and evaluated their refractometric sensing performance. The new MoM-CL technique was used for efficient fabrication of these "nanowell" nanostructures. We have focused on the situation where the metal film is very thin (tens of nm) and the dielectric film relatively thick (hundreds of nm). Using transfer matrix calculations, solutions of the surface wave dispersion relations and numerical simulations we have investigated the influence from different excitation mechanisms in the double film system. We have shown how the parameters such as dielectric layer thickness and hole periodicity can be tuned such that only plasmon resonances contribute to the optical spectrum. The approach summarized in this work should prove useful for future investigations of nanohole arrays in multilayered structures. For instance, the transfer matrix calculations are applicable to multilayers[4] and the dispersion relations in multilayers can also be expressed generically.[46] Furthermore, we have shown how the asymmetric field distribution results in an extremely low sensitivity in terms of redshifting for the surface plasmon. However, appropriate spectral analysis still provides high signal-to-noise upon molecular adsorption by monitoring either the localized mode shift or the coupling efficiency to the surface plasmons. We raise concerns about the use of the FoM to evaluate refractometric sensing performance.

As a future outlook, we suggest that these nanohole arrays in metal–dielectric double films can be used to analyze chemical phenomena in nanopores[56] and the behavior of molecules confined in nanoscale voids. For instance, one can envision functionalizing the Au with polymers or biological peptides and measure transport events through the pore opening into the nanowell below. If a single molecule is entrapped in the dielectric void, it represents a local concentration >1 μM, which implies interesting consequences, for example, for reaction kinetics. Further, our fabrication process can be directly transferred to Si_3N_4 membranes in order to construct flow-through devices with two separate liquid compartments.[29–31] Applications related to pore-spanning lipid membranes are particularly interesting in this case.[25] Overall, we suggest that the main

motivation of developing nanohole arrays for sensing applications is not to overcome the performance of SPR. Instead, the advantages lie in the unique geometry of the structure.

METHODS

Nanofabrication. Borosilicate glass (Menzel Gläser) was sonicated in acetone, isopropyl alcohol and H_2O before cleaning with microwave O_2 plasma for 5 min at 150 W and 1 mbar (Technics Plasma 100-E). Reactive sputtering was done with a Nb target and Ar + O_2 plasma (50% each) at 3.9×10^{-3} mbar and 200 W. The RI and thickness of the Nb_2O_5 films was measured by spectroscopic ellipsometry. Absorption in Nb_2O_5 was negligible (imaginary part of $n < 0.001$), strongly suggesting the amorphous pentoxide form.[43,44] Prior to colloid adsorption, the surface was cleaned with UV generated O_3 (UVOCS) for 15 min and exposed to a 5% solution of chlorohydrol (SummitReheis). Sulfate-stabilized polystyrene colloids (105 ± 4 nm and 152 ± 4 nm) were purchased from Microparticles GmbH. A 0.05% suspension was applied to the surface for ~2 min, followed by H_2O rinse, heating in ~130 °C ethylene glycol for ~5 s, H_2O rinse, and N_2 blow dry. Prior to metal deposition the chlorohydrol was removed by an additional 2 min of UV O_3 treatment, which also shrinks the colloids a few nanometers. Subsequently 30 nm Au and 20 nm Al_2O_3 was deposited by e-gun PVD (Leybold Univex 500). A pastry scrape was used for removing the colloids (squeegee liftoff) with the sample immersed in isopropyl alcohol. RIE was performed with 40 sccm CF_4 + 10 sccm O_2 at 18×10^{-3} mbar and 150 W (Oxford Instruments Plasmalab 80). Al_2O_3 was removed in a 30 mM NaOH solution[57] for ~1 h. Thermal annealing was done on a 250 °C hot plate in air. SEM imaging was done with a Zeiss Supra 60VP and a JEOL JEM7100F.

Simulations. The MMP simulations were conducted with OpenMax solver package (http://openmax.ethz.ch/). The edges were rounded by *ca.* 8 nm to avoid singularity. The extinction spectra were calculated from the efficiency of the Rayleigh expansions located at the bottom boundary.

Sensing Experiments. All chemicals were from Sigma unless stated otherwise and milli-Q water was used. Samples were first cleaned with RCA1 (1:1:5 volume mixture of 30% H_2O_2, 25% NH_3 and H_2O) at 60 °C for ~5 min, rinsed with H_2O, and dried with N_2. Passivation of Au with OEG (Prochimia) was done with a 1.5 mM solution in ethanol for ~2 h. NeutrAvidin (Pierce) adsorption was measured in 10 mM 4-(2-hydroxyethyl)-1-piperazineethanesulfonic acid with 150 mM NaCl and pH adjusted to 7.4.

Spectral Analysis. The centroids of the extinction maximum and minimum were calculated as described previously.[51,52] Extinction was defined as $\Omega = \log(I_0/I)$, where I_0 is reference intensity and I is measured intensity, using natural logarithms (*not* "absorbance", *i.e.* $\log_{10}$). The reference spectrum was recorded without the flow cell, which introduced a small constant offset in the spectra (no wavelength dependence). The dark spectrum was dynamically updated by a long pass filter.[51]

Conflict of Interest: The authors declare no competing financial interest.

Supporting Information Available: Description of waveguide mode calculations and the transfer matrix method. Spectra recorded during fabrication. Radial distribution functions for the colloid patterns. This material is available free of charge *via* the Internet at http://pubs.acs.org.

Acknowledgment. This work was funded by the Swedish Foundation for Strategic Research, the Swedish Research Council, Mizuho Foundation for the Promotion of Science, and the Swiss National Science Foundation. We thank Michael Horisberger at PSI for niobia coatings, Stephen Wheeler for making flow-cells, and the FIRST cleanroom staff.

REFERENCES AND NOTES

1. Gramotnev, D. K.; Bozhevolnyi, S. I. Plasmonics Beyond the Diffraction Limit. *Nat. Photon.* **2010**, *4*, 83–91.
2. Halas, N. J.; Lal, S.; Chang, W. S.; Link, S.; Nordlander, P. Plasmons in Strongly Coupled Metallic Nanostructures. *Chem. Rev.* **2011**, *111*, 3913–3961.
3. Stockman, M. I. Nanoplasmonics: Past, Present, and Glimpse Into Future. *Opt. Express* **2011**, *19*, 22029–22106.
4. Dahlin, A. B., *Plasmonic Biosensors: An Integrated View of Refractometric Detection*. IOS Press: Washington, DC, 2012.
5. Homola, J. Surface Plasmon Resonance Sensors for Detection of Chemical and Biological Species. *Chem Rev* **2008**, *108*, 462–493.
6. Zijlstra, P.; Paulo, P. M. R.; Orrit, M. Optical Detection of Single Non-absorbing Molecules Using the Surface Plasmon Resonance of a Gold Nanorod. *Nat. Nanotechnol.* **2012**, *7*, 379–382.
7. Englebienne, P. Use of Colloidal Gold Surface Plasmon Resonance Peak Shift to Infer Affinity Constants from the Interactions between Protein Antigens and Antibodies Specific for Single or Multiple Epitopes. *Analyst* **1998**, *123*, 1599–1603.
8. Jones, M. R.; Osberg, K. D.; Macfarlane, R. J.; Langille, M. R.; Mirkin, C. A. Templated Techniques for the Synthesis and Assembly of Plasmonic Nanostructures. *Chem. Rev.* **2011**, *111*, 3736–3827.
9. Lukyanchuk, B.; Zheludev, N. I.; Maier, S. A.; Halas, N. J.; Nordlander, P.; Giessen, H.; Chong, C. T. The Fano Resonance in Plasmonic Nanostructures and Metamaterials. *Nat. Mater.* **2010**, *9*, 707–715.
10. Verellen, N.; van Dorpe, P.; Huang, C. J.; Lodewijks, K.; Vandenbosch, G. A. E.; Lagae, L.; Moshchalkov, V. V. Plasmon Line Shaping Using Nanocrosses for High Sensitivity Localized Surface Plasmon Resonance Sensing. *Nano Lett.* **2011**, *11*, 391–397.
11. Kabashin, A. V.; Evans, P.; Pastkovsky, S.; Hendren, W.; Wurtz, G. A.; Atkinson, R.; Pollard, R.; Podolskiy, V. A.; Zayats, A. V. Plasmonic Nanorod Metamaterials for Biosensing. *Nat. Mater.* **2009**, *8*, 867–871.
12. Lodewijks, K.; van Roy, W.; Borghs, G.; Lagae, L.; van Dorpe, P. Boosting the Figure-of-Merit of LSPR-Based Refractive Index Sensing by Phase-Sensitive Measurements. *Nano Lett.* **2012**, *12*, 1655–1659.
13. Rich, R. L.; Myszka, D. G. Survey of the 2009 Commercial Optical Biosensor Literature. *J. Mol. Recognit.* **2011**, *24*, 892–914.
14. Dahlin, A. B. Size Matters: Problems and Advantages Associated with Highly Miniaturized Sensors. *Sensors* **2012**, *12*, 3018–3036.
15. Gordon, R.; Sinton, D.; Kavanagh, K. L.; Brolo, A. G.; New, A Generation of Sensors Based on Extraordinary Optical Transmission. *Acc. Chem. Res.* **2008**, *41*, 1049–1057.
16. Jonsson, M. P.; Dahlin, A. B.; Jonsson, P.; Hook, F. Nanoplasmonic Biosensing with Focus on Short-Range Ordered Nanoholes in Thin Metal Films. *Biointerphases* **2008**, *3*, Fd30–Fd40.
17. Masson, J. F.; Murray-Methot, M. P.; Live, L. S. Nanohole Arrays in Chemical Analysis: Manufacturing Methods and Applications. *Analyst* **2010**, *135*, 1483–1489.
18. Wittenberg, N. J.; Im, H.; Johnson, T. W.; Xu, X. H.; Warrington, A. E.; Rodriguez, M.; Oh, S. H. Facile Assembly of Micro- and Nanoarrays for Sensing with Natural Cell Membranes. *ACS Nano* **2011**, *5*, 7555–7564.
19. Dahlin, A. B.; Jonsson, M. P.; Hook, F. Specific Self-Assembly of Single Lipid Vesicles in Nanoplasmonic Apertures in Gold. *Adv. Mater.* **2008**, *20*, 1436–1442.
20. Wei, H.; Hakanson, U.; Yang, Z. L.; Hook, F.; Xu, H. X. Individual Nanometer Hole-Particle Pairs for Surface-Enhanced Raman Scattering. *Small* **2008**, *4*, 1296–1300.
21. Dahlin, A.; Zach, M.; Rindzevicius, T.; Kall, M.; Sutherland, D. S.; Hook, F. Localized Surface Plasmon Resonance

Sensing of Lipid-Membrane-Mediated Biorecognition Events. *J. Am. Chem. Soc.* **2005**, *127*, 5043–5048.
22. Marie, R.; Dahlin, A. B.; Tegenfeldt, J. O.; Hook, F. Generic Surface Modification Strategy for Sensing Applications Based on Au/SiO_2 Nanostructures. *Biointerphases* **2007**, *2*, 49–55.
23. Sannomiya, T.; Scholder, O.; Jefimovs, K.; Hafner, C.; Dahlin, A. B. Investigation of Plasmon Resonances in Metal Films with Nanohole Arrays for Biosensing Applications. *Small* **2011**, *7*, 1653–1663.
24. Ferreira, J.; Santos, M. J. L.; Rahman, M. M.; Brolo, A. G.; Gordon, R.; Sinton, D.; Girotto, E. M. Attomolar Protein Detection Using In-Hole Surface Plasmon Resonance. *J. Am. Chem. Soc.* **2008**, *131*, 436–437.
25. Im, H.; Wittenberg, N. J.; Lesuffleur, A.; Lindquist, N. C.; Oh, S. H. Membrane Protein Biosensing with Plasmonic Nanopore Arrays and Pore-Spanning Lipid Membranes. *Chem Sci* **2010**, *1*, 688–696.
26. Dahlin, A. B.; Jonsson, P.; Jonsson, M. P.; Schmid, E.; Zhou, Y.; Hook, F. Synchronized Quartz Crystal Microbalance and Nanoplasmonic Sensing of Biomolecular Recognition Reactions. *ACS Nano* **2008**, *2*, 2174–2182.
27. Dahlin, A. B.; Sannomiya, T.; Zahn, R.; Sotiriou, G. A.; Voros, J. Electrochemical Crystallization of Plasmonic Nanostructures. *Nano Lett* **2011**, *11*, 1337–1343.
28. Dahlin, A. B.; Zahn, R.; Voros, J. Nanoplasmonic Sensing of Metal-Halide Complex Formation and the Electric Double Layer Capacitor. *Nanoscale* **2012**, *4*, 2339–2351.
29. Eftekhari, F.; Escobedo, C.; Ferreira, J.; Duan, X. B.; Girotto, E. M.; Brolo, A. G.; Gordon, R.; Sinton, D. Nanoholes as Nanochannels: Flow-Through Plasmonic Sensing. *Anal. Chem.* **2009**, *81*, 4308–4311.
30. Jonsson, M. P.; Dahlin, A. B.; Feuz, L.; Petronis, S.; Hook, F. Locally Functionalized Short-Range Ordered Nanoplasmonic Pores for Bioanalytical Sensing. *Anal. Chem.* **2010**, *82*, 2087–2094.
31. Yanik, A. A.; Huang, M.; Artar, A.; Chang, T. Y.; Altug, H. Integrated Nanoplasmonic-Nanofluidic Biosensors with Targeted Delivery of Analytes. *Appl. Phys. Lett.* **2010**, *96*, 021101.
32. Ebbesen, T. W.; Lezec, H. J.; Ghaemi, H. F.; Thio, T.; Wolff, P. A. Extraordinary Optical Transmission through Subwavelength Hole Arrays. *Nature* **1998**, *391*, 667–669.
33. Garcia-Vidal, F. J.; Martin-Moreno, L.; Ebbesen, T. W.; Kuipers, L. Light Passing through Subwavelength Apertures. *Rev. Mod. Phys.* **2010**, *82*, 729–787.
34. Feuz, L.; Jonsson, P.; Jonsson, M. P.; Hook, F. Improving the Limit of Detection of Nanoscale Sensors by Directed Binding to High-Sensitivity Areas. *ACS Nano* **2010**, *4*, 2167–2177.
35. Jonsson, M. P.; Jonsson, P.; Dahlin, A. B.; Hook, F. Supported Lipid Bilayer Formation and Lipid-Membrane-Mediated Biorecognition Reactions Studied with a New Nanoplasmonic Sensor Template. *Nano Lett.* **2007**, *7*, 3462–3468.
36. Beines, P. W.; Klosterkamp, I.; Menges, B.; Jonas, U.; Knoll, W. Responsive Thin Hydrogel Layers from Photo-Cross-Linkable Poly(*N*-isopropylacrylamide) Terpolymers. *Langmuir* **2007**, *23*, 2231–2238.
37. Chen, H. M.; Pang, L.; Kher, A.; Fainman, Y. Three-Dimensional Composite Metallodielectric Nanostructure for Enhanced Surface Plasmon Resonance Sensing. *Appl. Phys. Lett.* **2009**, *94*, 073117.
38. Najiminaini, M.; Vasefi, F.; Kaminska, B.; Carson, J. J. L. Nanohole Array Structure with Improved Surface Plasmon Energy Matching Characteristics. *Appl. Phys. Lett.* **2012**, *100*, 043105.
39. Zhang, X. M.; Li, Z. B.; Ye, S. S.; Wu, S.; Zhang, J. H.; Cui, L. Y.; Li, A. R.; Wang, T. Q.; Li, S. Z.; Yang, B. Elevated Ag Nanohole Arrays for High Performance Plasmonic Sensors Based on Extraordinary Optical Transmission. *J. Mater. Chem.* **2012**, *22*, 8903–8910.
40. Pacifici, D.; Lezec, H. J.; Sweatlock, L. A.; Walters, R. J.; Atwater, H. A. Universal Optical Transmission Features in Periodic and Quasiperiodic Hole Arrays. *Opt. Express* **2008**, *16*, 9222–9238.
41. Przybilla, F.; Genet, C.; Ebbesen, T. W. Long *vs* Short-Range Orders in Random Subwavelength Hole Arrays. *Opt. Express* **2012**, *20*, 4697–4709.
42. Prikulis, J.; Hanarp, P.; Olofsson, L.; Sutherland, D.; Kall, M. Optical Spectroscopy of Nanometric Holes in Thin Gold Films. *Nano Lett.* **2004**, *4*, 1003–1007.
43. Lai, F. C.; Li, M.; Wang, H. Q.; Hu, H. L.; Wang, X. P.; Hou, J. G.; Song, Y. Z.; Jiang, Y. S. Optical Scattering Characteristic of Annealed Niobium Oxide Films. *Thin Solid Films* **2005**, *488*, 314–320.
44. Venkataraj, S.; Drese, R.; Liesch, C.; Kappertz, O.; Jayavel, R.; Wuttig, M. Temperature Stability of Sputtered Niobium-Oxide Films. *J. Appl. Phys.* **2002**, *91*, 4863–4871.
45. Tiefenthaler, K.; Lukosz, W. Sensitivity of Grating Couplers as Integrated-Optical Chemical Sensors. *J. Opt. Soc. Am., B* **1989**, *6*, 209–220.
46. Ward, C. A.; Bhasin, K.; Bell, R. J.; Alexander, R. W.; Tyler, I. Multimedia Dispersion-Relation for Surface Electromagnetic-Waves. *J. Chem. Phys.* **1975**, *62*, 1674–1676.
47. Etchegoin, P. G.; Le Ru, E. C.; Meyer, M. An Analytic Model for the Optical Properties of Gold. *J. Chem. Phys.* **2006**, *125*, 164705.
48. Johnson, P. B.; Christy, R. W. Optical-Constants of Noble-Metals. *Phys. Rev. B* **1972**, *6*, 4370–4379.
49. Brian, B.; Sepulveda, B.; Alaverdyan, Y.; Lechuga, L. M.; Kall, M. Sensitivity Enhancement of Nanoplasmonic Sensors in Low Refractive Index Substrates. *Opt. Express* **2009**, *17*, 2015–2023.
50. Park, T. H.; Mirin, N.; Lassiter, J. B.; Nehl, C. L.; Halas, N. J.; Nordlander, P. Optical Properties of a Nanosized Hole in a Thin Metallic Film. *ACS Nano* **2008**, *2*, 25–32.
51. Dahlin, A. B.; Tegenfeldt, J. O.; Hook, F. Improving the Instrumental Resolution of Sensors Based on Localized Surface Plasmon Resonance. *Anal. Chem.* **2006**, *78*, 4416–4423.
52. Dahlin, A. B.; Chen, S.; Jonsson, M. P.; Gunnarsson, L.; Kall, M.; Hook, F. High-Resolution Microspectroscopy of Plasmonic Nanostructures for Miniaturized Biosensing. *Anal. Chem.* **2009**, *81*, 6572–6580.
53. Sannomiya, T.; Balmer, T. E.; Hafner, C.; Heuberger, M.; Voros, J. Optical Sensing and Determination of Complex Reflection Coefficients of Plasmonic Structures Using Transmission Interferometric Plasmonic Sensor. *Rev. Sci. Instrum.* **2010**, *81*, 053102.
54. Yanik, A. A.; Cetin, A. E.; Huang, M.; Artar, A.; Mousavi, S. H.; Khanikaev, A.; Connor, J. H.; Shvets, G.; Altug, H. Seeing Protein Monolayers with Naked Eye through Plasmonic Fano Resonances. *Proc. Natl. Acad. Sci. U.S.A.* **2011**, *108*, 11784–11789.
55. Dahlin, A. B.; Jonsson, M. P. Performance of Nanoplasmonic Biosensors. In *Nanoplasmonic Sensors*; Dmitriev, A., Ed.; Springer: New York, 2012; pp 231−265.
56. Tagliazucchi, M.; Szleifer, I. Stimuli-Responsive Polymers Grafted to Nanopores and Other Nano-curved Surfaces: Structure, Chemical Equilibrium and Transport. *Soft Matter* **2012**, *8*, 7292–7305.
57. McPhillips, J.; Murphy, A.; Jonsson, M. P.; Hendren, W. R.; Atkinson, R.; Hook, F.; Zayats, A. V.; Pollard, R. J. High-Performance Biosensing Using Arrays of Plasmonic Nanotubes. *ACS Nano* **2010**, *4*, 2210–2216.